



HAL
open science

Influence of following, regular and irregular long waves on wind-wave growth with fetch: an experimental study

Antoine Villefer, Michel Benoit, Damien Violeau, Christopher Luneau, Hubert Branger

► To cite this version:

Antoine Villefer, Michel Benoit, Damien Violeau, Christopher Luneau, Hubert Branger. Influence of following, regular and irregular long waves on wind-wave growth with fetch: an experimental study. *Journal of Physical Oceanography*, 2021, 51 (11), pp.3435-3448. 10.1175/JPO-D-21-0050.1 . hal-03345981

HAL Id: hal-03345981

<https://hal.science/hal-03345981>

Submitted on 6 May 2022

HAL is a multi-disciplinary open access archive for the deposit and dissemination of scientific research documents, whether they are published or not. The documents may come from teaching and research institutions in France or abroad, or from public or private research centers.

L'archive ouverte pluridisciplinaire **HAL**, est destinée au dépôt et à la diffusion de documents scientifiques de niveau recherche, publiés ou non, émanant des établissements d'enseignement et de recherche français ou étrangers, des laboratoires publics ou privés.

1 **Influence of following, regular and irregular long waves on wind-wave**
2 **growth with fetch: an experimental study**

3 Antoine Villefer*

4 *EDF R&D / LNHE, 78400 Chatou, France*

5 *Laboratory for Hydraulics Saint-Venant, 78400 Chatou, France*

6 *Aix Marseille Univ, CNRS, Centrale Marseille, Institut de Recherche sur les Phénomènes*

7 *Hors-Equilibre (IRPHE, UMR 7342), 13013 Marseille, France*

8 Michel Benoit

9 *EDF R&D / LNHE, 78400 Chatou, France*

10 *Aix Marseille Univ, CNRS, Centrale Marseille, Institut de Recherche sur les Phénomènes*

11 *Hors-Equilibre (IRPHE, UMR 7342), 13013 Marseille, France*

12 Damien Violeau

13 *EDF R&D / LNHE, 78400 Chatou, France*

14 *Laboratory for Hydraulics Saint-Venant, 78400 Chatou, France*

15 Christopher Luneau

16 *Institut Pythéas, Aix Marseille Univ, CNRS, IRD, 13009 Marseille, France*

17 Hubert Branger

18 *Aix Marseille Univ, CNRS, Centrale Marseille, Institut de Recherche sur les Phénomènes*
19 *Hors-Equilibre (IRPHE, UMR 7342), 13013 Marseille, France*

20 **Corresponding author: Antoine Villefer, antoine.villefer@edf.fr*

ABSTRACT

21 A series of experiments were conducted in a wind-wave tank facility in Marseilles (France) to study
22 the effects of preexisting swell conditions (represented by long mechanically-generated waves) on
23 wind-wave growth with fetch. Both monochromatic and irregular (JONSWAP-type) long wave
24 conditions with different values of wave steepness have been generated in the presence of a constant
25 wind forcing, for several wind velocities. A spectral analysis of temporal wave signals combined
26 with airflow measurements allowed to study the evolution of both wave systems with the aim of
27 identifying the interaction mechanisms transportable to prototype scale. In particular, a specific
28 method is used to separate the two wave systems in the measured bimodal spectra. In fetch-limited
29 conditions, pure wind-wave growth is in accordance with anterior experiments, but differs from
30 the prototype scale in terms of energy and frequency variations with fetch. Monochromatic long
31 waves are shown to reduce the energy of the wind-waves significantly, as it was observed in anterior
32 laboratory experiments. The addition of JONSWAP-type long waves instead results in a downshift
33 of the wind-wave peak frequency but no significant energy reduction. Overall, it is observed that
34 the presence of long waves affects the wind-wave energy and frequency variations with fetch.
35 Finally, in the presence of JONSWAP-type long waves, variations of wind-wave energy and peak
36 frequency with fetch appear in close agreement with the wind-wave growth observed at prototype
37 scale both in terms of variations and nondimensional magnitude.

38 **1. Introduction**

39 The infinite diversity of waves in the ocean makes the understanding of the complex sea-states
40 dynamics rather difficult. Numerous experimental studies both in the field and in laboratories
41 have been carried out over the last decades to improve the knowledge on the particular case of
42 bimodal sea-states or more precisely on wind-wave and swell combination. Many field measure-
43 ments (Donelan et al. 1997; Hwang et al. 2011; Vincent et al. 2019) show evidence of a modified
44 wind-wave generation in the presence of swell. However, field experiments can hardly be gen-
45 eralized due to the specific wind and atmospheric conditions varying from one experiment to
46 another. In wind-wave tank facilities, wind-wave and swell combination can be studied in con-
47 trolled conditions using a wave-maker (e.g. a mechanically actuated paddle) for representing swell
48 and a closed-loop air circulation to produce a quality airflow creating short wind-waves above the
49 long mechanically-generated waves (paddle-waves). Thereby, both wave systems are sufficiently
50 separated in frequency to observe a bimodal sea-state. A series of experiments was conducted in
51 a well-controlled laboratory environment in Marseilles (France) with two objectives. The first one
52 was to identify the mechanisms at stake in the interaction between the two wave systems. Assessing
53 the extent at which those mechanisms can be transposed to wind-wave growth in the ocean was the
54 second objective.

55 The wind-wave generation over a train of long monochromatic paddle-waves propagating along
56 the wind direction is a well-documented experimental configuration (Mitsuyasu 1966; Phillips and
57 Banner 1974; Donelan 1987). In these conditions, a drastic reduction on the energy density of the
58 wind-wave component is unanimously observed. The intensity of this reduction increases with the
59 long-wave steepness ak (where a is the wave amplitude and k the wave number). Donelan (1987)
60 found a windsea elevation variance reduced by a factor of about 2.5 in presence of long waves. A

61 similar experiment by Mitsuyasu and Yoshida (1991) with long waves propagating opposite to the
 62 wind direction revealed wind-wave height intensification. More recently, Benetazzo et al. (2019)
 63 and Bailey et al. (2020) carried out experiments (in an open-air basin without a closed-loop airflow
 64 in the case of Bailey et al.) on wind over irregular (JONSWAP-type) paddle-waves. These latter
 65 experiments also showed a reduced wind-wave growth.

66 Variance density spectrum $E(f, \theta, x, t)$, with f and θ are respectively the wave frequency and
 67 direction, is a powerful manner to describe wind-wave growth. For infinite depth, the evolution of
 68 $E(f, \theta, x, t)$ is governed by the spectral energy balance involving source/sink terms $S(f, \theta, x, t)$:

$$\frac{dE}{dt} = S_{in} + S_{ds} + S_{nl} \quad (1)$$

69 The left hand side is the kinematic part of the equation while the right hand side includes three
 70 source/sink terms corresponding to wind energy input S_{in} , dissipation through white-capping S_{ds}
 71 and nonlinear four-wave interactions S_{nl} .

72 Experiments of wind over monochromatic mechanically-generated waves propagating in the same
 73 direction have received a lot of attention to provide a physical explanation to wind-wave reduction
 74 and to consider at what extent this effect could appear at natural scale. First, the hypothesis of
 75 an enhanced wave breaking of the windsea, represented by S_{ds} , due to the addition of wind drift
 76 and long-wave orbital velocities, was suggested by Phillips and Banner (1974). This suggestion
 77 was later shaded by Wright (1976) arguing that enhanced wave breaking could not account for
 78 the magnitude of wind-wave reduction in the case of high wind velocities. According to Masson
 79 (1993), nonlinear four-wave interactions (i.e. S_{nl}) is also involved in the physical evolution when
 80 the ratio of long waves over short-waves frequencies is greater than 0.6. This ratio discriminates
 81 the interaction between wind-waves and swell in the ocean (ratio lower than 0.6) and in most
 82 laboratory experiments (ratio greater than 0.6).

83 Chen and Belcher (2000) developed a model based on a sheltering effect of the long waves
84 absorbing momentum from the wind, thus reducing the available momentum for wind-wave gen-
85 eration (i.e. S_{in}). Their model delivered results in accordance with laboratory experiments but
86 closely depending on the growth rate coefficient β formulated by Miles (1957) as $S_{in} = \beta E$, which
87 is known to be highly variable, especially at laboratory scale. The growth rate coefficient itself de-
88 pends on the long-wave age, C/u_{\star} , with C the long-wave (phase) celerity, $u_{\star} = (\tau/\rho)^{1/2}$ the friction
89 velocity, τ the total turbulent shear stress and ρ the air density. Chen and Belcher's results suggest
90 that the wind-wave reduction observed in laboratory environment with young waves ($C/u_{\star} \ll 20$)
91 would probably not occur with older ocean swell for which $C/u_{\star} > 20$. More directly, Chen and
92 Belcher's model predicts that the sheltering effect occurs when the long waves are, to a good extent,
93 slower than the wind. Lately, Donelan et al. (2010) attributed the wind-wave reduction to both the
94 modified airflow (i.e. S_{in}) and the orbital velocity gradients in the presence of the long waves.

95 In our experiment, short waves were generated by the wind in a large closed-loop wind/wave
96 tank facility, and long waves were generated with a wave-maker, with both cases of monochromatic
97 waves and irregular (JONSWAP-type) waves. All the measurements were carried out on a fetch-
98 limited wave field. The fetch limited case is a generic case of spatial wave evolution consisting in
99 a steady wind forcing over a statistically stationary wave-field. The statistical wave-field can be
100 related to the wave-spectrum notion.

101 In order to compare our experimental results with other laboratory experiments and field obser-
102 vations, an appropriate scaling has to be applied. Following Kitaigorodskii (1961), the parameters
103 describing wind-wave growth are the total variance of the free-surface elevation $m_0 = \overline{\eta^2}$ and the
104 peak frequency f_p as a function of the fetch X . Those variables are made dimensionless using the

105 friction velocity u_\star and the acceleration due to gravity g :

$$f_p^* = \frac{f_p u_\star}{g} \quad (2)$$

$$m_0^* = \frac{m_0 g^2}{u_\star^4} \quad (3)$$

$$X^* = \frac{Xg}{u_\star^2} \quad (4)$$

108 Although the wind speed 10 m above the mean free surface $U_{10} = U(z = 10 \text{ m})$ is usually employed
109 as a scaling wind speed, the friction velocity is chosen here since it does not depend on height and
110 it better represents the momentum transfer at the air/water interface (Janssen 2004).

111 The facility and the data processing methods are introduced in Section 2. The wind profiles
112 determined in presence and in absence of paddle-waves, used as a scaling tool for the subsequent
113 analyses, are presented in section 3. The growth of wind-waves is measured and processed in
114 absence of long waves in section 4, then in presence of monochromatic waves in section 5 and
115 finally with irregular waves in section 6. A comparison of these different cases and their relation
116 with the prototype scale are discussed in section 7. Section 8 gives a summary of results and their
117 application, followed by a further discussion on future studies on the topic.

118 **2. Experimental Facility and Data Processing**

119 *a. The Facility*

120 The IRPHÉ/Pythéas wind-wave tank, sketched in Figure 1, consists of a closed-loop tunnel
121 for air circulation with a 1.5-m-high air cavity above a basin with a test section 40-m-long and
122 2.60-m-wide. The water depth h , set to 0.80 m, was kept constant during all the experiments. For
123 a complete description of the facility, one can refer to Coantic et al. (1981). The wind is generated
124 by an air blower in the upper part of the tunnel and guided through a settling chamber with a
125 honeycomb and a converging nozzle ; this system produces a uniform airflow at the entrance of

126 the water basin. At the upwind end of the basin, an immersed paddle wave-maker (piston-type)
127 can be used for generating either monochromatic or irregular waves propagating along the wind
128 direction. At the downwind end, a permeable absorbing beach with a 6-degrees-slope was installed
129 to minimize wave reflection. The basin side walls are punctuated with windows to observe the
130 water surface. A larger 5-m-long clear glass is situated at the 25-m-fetch to perform measurements
131 that require a sight on the water surface.

132 For these experiments, eight resistance-type and four capacitance-type wave gauges were dis-
133 tributed along the basin to measure the instantaneous free surface elevation η (Figure 1). Two
134 anemometers were situated in front of the clear glass at a 25-m-fetch (Figure 1). Wind reference
135 velocity U_{ref} was measured at approximately 0.5 m above the water surface with a Gill 2D sonic
136 anemometer. An additional hot film anemometer from E+E Elektronik supported by a vertical
137 telescopic pole allowed to measure the vertical profile of the mean (i.e. time averaged) horizontal
138 velocity $U(z)$. Friction velocity and aerodynamic roughness z_0 are determined by fitting the log-
139 arithmic profile (see Section 3) to the vertical time-averaged wind profile in neutral atmospheric
140 conditions for all the experiments (air and water were roughly at the same temperature). The
141 friction velocity is considered constant along the test section because of the slightly divergence of
142 the air section along the wind-wave tank allowing a zero pressure longitudinal gradient.

143 Apart from the air blower controlled with a graduated potentiometer, the control of the wave-
144 maker and all the gauges output signals were gathered on a computer using a LabView program.
145 Wind velocity could be generated between 2 and 14 $\text{m}\cdot\text{s}^{-1}$ (U_{ref}) by regulating the potentiometer.
146 In order to generate waves, the required temporal free surface elevation was convoluted with the
147 wave-maker transfer function, and then transferred as a voltage signal from the computer to the
148 piston wave-maker, converting the input signal to actual waves. Both regular (Stokes-type) and

149 irregular (JONSWAP-type) wave trains were generated. The JONSWAP spectrum is given by:

$$E(f) = \alpha_p H_s^2 \frac{f_p^4}{f^5} \exp \left[-\frac{5}{4} \left(\frac{f_p}{f} \right)^4 \right] \gamma \exp \left[-\frac{(f-f_p)^2}{2\sigma^2 f_p^2} \right] \quad (5)$$

150 where, using the JONSWAP's recommendations (Hasselmann et al. 1973), $\sigma = 0.07$ for $f < f_p$ and
151 $\sigma = 0.09$ for $f > f_p$, $\gamma = 3.3$ is the peak enhancement factor and $\alpha_p = 0.2$ is the Phillips constant.
152 The significant wave height H_s and the peak frequency f_p are the parameters to adjust in order to
153 obtain the desired sea-state.

154 To generate the time series of irregular waves, inverse FFT (Fast Fourier Transform) transforms
155 of the complex amplitudes from the JONSWAP spectra (using random phases) were used over
156 the frequency range [0.4-4.0] Hz. This wide range of frequency, which is the recommended
157 mechanical range for the wavemaker, was necessary in order to obtain a smooth transition between
158 the JONSWAP peak and the high frequency waves. However, the wave-maker was able to accurately
159 generate a sea-state corresponding to a JONSWAP-type spectrum over the frequency range [0.4-2.0]
160 Hz. Above 2 Hz the energy distribution could slightly deviate from the f^{-5} desired tail.

161 Acquisition of wave gauges signals were launched from the computer for a 20 minutes duration
162 at the sampling rate 256 Hz. Before every acquisition, it was verified that the waves in the wave
163 tank were in stationary fetch-limited conditions by waiting a sufficient long time before acquiring
164 data. During the experiments with wind, the instantaneous horizontal wind velocity was measured
165 using the hot film anemometer from the lower point above the water surface (i.e. slightly above
166 the highest wave) at about ten vertically distributed points over a range of 20 cm and a duration
167 of 240 s to obtain the vertical profile of the mean horizontal velocity. In order to be able to
168 differentiate swell from wind-waves, the mechanically-generated wave frequency (respectively the
169 peak frequency for irregular waves) was chosen equal to 0.6 Hz. This choice accounts for the
170 wind-waves lower peak frequency reaching 1 Hz at maximum fetch and maximum wind velocity.

171 Using the dispersion relation for the long waves, the non-dimensional depth $kh = 1.33$ corre-
172 sponds to intermediate water depth. Thus, bottom friction slightly dissipates the paddle-waves as
173 they propagate along the tank. Bottom friction and additionnal dissipation mechanisms, such as
174 sidewalls friction, that occur in laboratory experiments have been quantified using Dorn's formula
175 (Dorn 1966). At the downwind end of the tank, more than 95 % of the long wave energy is con-
176 served. Wind-waves, however, are short enough ($kh > 3$) to be considered as propagating in deep
177 water and unaffected by bottom friction. Wind-wave dissipation by sidewalls remains weak since
178 their wavelenghts is much smaller than the channel width (Shemer 2019). Overall, the dissipation
179 due to bottom and sidewalls friction is relatively low and is not further considered in the present
180 study.

181 Table 1 gathers the characteristics of all the tests presented in this paper.

182 *b. Spectral Separation Methods*

183 A spectral approach was chosen to characterize the interaction between wave systems. Spectra
184 were calculated using the Welch method by partitioning the surface elevation time records into
185 shorter records of 16384 points with a 50 % overlap and a Hanning windowing. Depending on the
186 sea-states, the resulting spectra were unimodal (wind-waves only, irregular swell only) or multi-
187 modal (monochromatic swell with harmonics, swell and wind-waves combination). Separating
188 wave systems in multi-modal sea-states is necessary to have access to their individual characteristics
189 (e.g. significant wave height, peak period, spectral width) in order to compare windsea growth with
190 and without swell for instance. In the literature, this separation is commonly performed using a
191 transition frequency that divides the wave spectrum in two parts: swell and windsea. That method
192 works while the peaks of both wave systems are sufficiently separated. In some cases, as it will be
193 shown in this paper, windsea and swell components are overlapping, making difficult the separation

194 with the former method. Two methods to separate the mechanically-generated wave part from the
195 wind-wave part of multi-modal spectra are introduced in this section. The first method deals with
196 the multi-modal sea-states with a monochromatic swell. The second method refers to multi-modal
197 sea-states with a JONSWAP-type swell. Both methods are based on curve-fitting using a nonlinear
198 least square method, and are described below.

199 The generation of monochromatic long waves with the wave-maker leads to the generation of
200 additional super-harmonic waves in intermediate depth conditions. These harmonics occupy the
201 same frequency range as the windsea making difficult the distinction between the proper energies
202 and peak frequencies of these overlapping systems. The first stage of the method consists in the
203 removal of the spectral bands containing the frequencies of the monochromatic wave harmonics
204 into the initially measured multi-modal spectrum. The removed number of points is arbitrary and
205 depends upon the width of the corresponding harmonic peaks. Thus, although the wind-wave
206 peak then becomes discontinuous at this stage, its shape is conserved. The next stage is to fit
207 the discontinuous wind-wave spectral peak with a JONSWAP-type spectrum initialized with the
208 triplet $(f_p, H_s, \gamma = 3.3)$. The initial value of the significant wave height H_s is equal to the integral
209 of the spectrum and the initial peak frequency f_p is equal to the maximum value of the spectrum.
210 The fitted JONSWAP-type spectrum enables to access the energy and the peak frequency of the
211 wind-wave part of the spectrum. Then, the harmonic-only part of the spectrum can be obtained by
212 subtracting the wind-wave part from the initially measured multi-modal spectrum.

213 A spectrum combining irregular-swell and wind-waves can be decomposed using the following
214 procedure inspired from Mackay (2011). First, a unimodal JONSWAP-type spectrum E^+ (see
215 (5)) is fitted on the bimodal measured spectrum E_m using the triplet $(f_p^+, H_s^+, \gamma^+ = 3.3)$ as initial
216 values: H_s^+ is determined using the integral of E_m and f_p^+ is equal to the frequency of the higher
217 peak. For this first fit, the peak frequency is a constant parameter in order to fit the higher peak

218 only. The resulting fitted triplet is $(f_p^+, H_s^{+'}, \gamma^{+'})$ (the prime denoting the fitted parameters). A
 219 second triplet $(f_p^-, H_s^-, \gamma^- = 3.3)$ is used as initial value for the second (i.e. the lower) peak with
 220 H_s^- from the integral of $E^- = E_m - E^+$ and f_p^- as the peak frequency of E^- . The sum of two
 221 JONSWAP-type spectra (i.e. bimodal) $E^- + E^+$ is fitted on the bimodal measured spectrum E_m
 222 using (f_p^-, H_s^-, γ^-) and $(f_p^+, H_s^{+'}, \gamma^{+'})$ as initial values. Thus, the measured spectrum is decomposed
 223 in two JONSWAP-type spectra permitting to determine the energy and peak frequency of each
 224 wave system.

225 An illustration of the spectral separation of a measured bimodal spectrum is given in Figure
 226 2. The figure shows that the spectra resulting from the spectral separation are an accurate fit for
 227 both long-wave and wind-wave peaks but slightly deviate from the measured spectrum in the high
 228 frequency range. It is also interesting to note the slight reduction of wind-wave energy at the
 229 peak of the wind-wave spectrum whether the spectrum is separated or included in the bimodal
 230 spectrum. This last observation proves the necessity of a proper separation of each wave system
 231 in a multi-modal measured spectrum so that they can be compared to the wave systems observed
 232 individually in unimodal measured spectra as it will be performed in the following.

233 3. Estimation of the Vertical Wind Profile

234 Among the numerous methods for estimating wind fluxes, the profile method was used for this
 235 experiment. Thus, the airflow above water waves is considered analogous to that above a stationary
 236 rough surface. Assuming a constant flux layer and using the Monin and Obukhov (1954) turbulence
 237 similarity theory, the vertical velocity wind profile is assumed logarithmic and may be written as:

$$U(z) = \frac{u_{\star}}{\kappa} \ln \left(\frac{z}{z_0} \right) \quad (6)$$

238 where $\kappa = 0.41$ is the von Karman constant and z_0 is the aerodynamic roughness. The measured
239 vertical evolution of the mean horizontal wind velocity is fitted with the logarithmic turbulent
240 velocity profile (6). In that way, the friction velocity and the aerodynamic roughness are found for
241 cases with and without paddle-waves.

242 Figure 3 displays the vertical profiles of the averaged horizontal wind velocity with and without
243 paddle-waves, for monochromatic and irregular waves. The measured wind velocities have an
244 overall tendency to increase when paddle-waves are present. Regarding the fitted logarithmic
245 profiles, paddle-waves have a trend to increase the friction velocity, thus inducing an increase in
246 the total shear stress τ at the air/water interface. Those results are in disagreement with Chen and
247 Belcher (2000) who designed a model for the reduction of wind-waves due to long monochromatic
248 waves based on the absence of variation of the total stress with long-wave steepness.

249 However, the large error-bars corresponding to the standard deviation in the calculation of the
250 mean horizontal velocity depicted in Figure 3 show the uncertainties associated with the logarithmic
251 fit. Thus, there is a high degree of uncertainty in the estimation of u_\star . Regarding the measurements,
252 two evaluations of the friction velocity in the same experimental conditions could lead to a 20 %
253 variation in the results. Additionally, water sprays at high wind speed (e.g. $U_{\text{ref}} = 14 \text{ m.s}^{-1}$)
254 could invalidate the measurements by reaching the hot film and cooling down its temperature, thus
255 measuring abnormally high velocities. Overall, the logarithmic profile is prone to be criticized for
256 a wind-over-long-wave use.

257 Due to the uncertainties previously mentioned, the measured data will be scaled using a unique
258 friction velocity for each wind speed. This friction velocity is determined using the profile method
259 on pure windsea cases (see Figure 3). Thus, the measurement uncertainties added by the presence
260 of long waves are avoided, but possible effects of such waves on the wind friction velocity will be
261 ignored. Shemer (2019) observed that the friction velocity does not depend notably on the fetch

262 in a similar fetch-limited case. Using this latter observation in our study, the friction velocity is
 263 assumed to be constant along the fetch with an impact of the surface drift velocity considered as
 264 negligible (Shemer 2019).

265 **4. Wind-Wave Growth**

266 This section aims to verify the similarities on fetch-limited wind-wave growth between our
 267 results, anterior laboratory experiments and ocean measurements. In this section, experimental
 268 data with wind only (i.e. without mechanically-generated waves) are analyzed.

269 Laboratory experiments are, on one hand, necessary to facilitate the understanding of wind-wave
 270 growth through controlled conditions. On the other hand, limitations are present due the limited
 271 size and the peculiarities from a wave tank to another. To quantify these limitations, fetch-limited
 272 cases of wind-wave growth under four increasing wind velocities have been carried out in the
 273 wind-wave tank. In Figure 4, the evolution of the measured dimensionless wind-wave energy and
 274 peak frequency are plotted and compared to two selected empirical laws. The first one is Mitsuyasu
 275 and Rikiishi (1978) law exclusively based on laboratory experiments:

$$m_0^* = 4.49 \times 10^{-5} (X^*)^{1.282} \quad \text{and} \quad f_p^* = 1.19 (X^*)^{-0.357} \quad (7)$$

276 The second one is Kahma and Calkoen (1992) law for stable stratification (adapted to friction
 277 velocity scaling from Komen et al. (1994)) obtained from a collection of laboratory and ocean data:

$$m_0^* = 7.3 \times 10^{-4} (X^*)^{0.85} \quad \text{and} \quad f_p^* = 0.477 (X^*)^{-0.26} \quad (8)$$

278 Figure 4 shows the differences in wind-wave growth depending on the wind speed in our experi-
 279 ments. At high wind speed, $U_{\text{ref}} \geq 10 \text{ m.s}^{-1}$, energy and peak frequency exhibit a linear evolution

280 with fetch in log-log coordinates confirming a power law behavior. Additionally, this power law
281 appears to be in accordance with Mitsuyasu and Rikiishi (1978)'s law.

282 At lower wind speed, water surface tension affects the evolution of wind-wave energy, especially
283 because most of the waves are short, hence in the capillary-gravity range, where surface tension
284 strongly modifies the wave dynamics. The case $U_{\text{ref}} = 6 \text{ m.s}^{-1}$ is characterized by a two-stage
285 evolution that clearly appears in the energy variation: the first stage, $X^* < 10^3$, shows a strong
286 slope which is attenuated, in a second stage, at larger fetches. Surface tension impact thus decreases
287 gradually as the waves grow. The second stage, $X^* > 10^3$, is linear and parallel to Mitsuyasu and
288 Rikiishi's power law indicating that the surface tension effect on waves is lower. Wind-waves
289 generated by a 4 m.s^{-1} wind deviate markedly from both the experimental curves for higher wind
290 speeds and empirical laws: surface tension seems to have a significant effect in that case.

291 Moreover, both dimensionless energy and peak frequency magnitudes agree reasonably well with
292 Kahma and Calkoen's law. The differences with this latter law lie in the variations of the variables
293 with fetch. Since Mitsuyasu and Rikiishi's law is a good fit for our experimental data variations,
294 absolute value of the power coefficients from Kahma and Calkoen's law (0.85 for the energy, 0.26
295 for the peak frequency in (8)) appear somewhat too low to accurately describe laboratory data
296 (corresponding exponents are 1.282 for the energy, 0.357 for the peak frequency in (7)). Recently,
297 Shemer (2019) also fitted power laws to a set of small-scale experiments, and found exponents in
298 rather good agreement with the values obtained here, namely 1.012 for the energy and 0.27 for the
299 peak frequency.

300 Another relevant comparison with empirical law can be done using Toba's 3/2 law (Toba 1997):

$$H_s^* = 0.062(f_p^*)^{3/2} \quad (9)$$

301 or in term of energy formulation

$$m_0^* = 2.4 \times 10^{-4} (f_p^*)^3 \quad (10)$$

302 This law is well adapted to ocean measurements. Contrary to power law previously mentioned the
303 fetch does not appear in this relation. This is a benefit since the fetch is difficult to define in the
304 real ocean because of the wind changing speed and direction. Note that the previous two sets of
305 laws (7) and (8) disagree with (10) in the sense that the ratio of their power coefficients is slightly
306 above the value of 3 as claimed by Toba.

307 Figure 5 shows the agreement between our experimental results and Toba's law. In line with
308 Figure 4, once wind-waves are long enough to be free from surface tension effect (i.e. below a
309 certain peak frequency or above a certain wind speed) Toba's law is well adapted to describe our
310 experimental data set.

311 This section proved that laboratory experiments are, to a good extent, appropriate to describe
312 short fetch evolution of a growing windsea in the ocean. From this observation, long mechanically-
313 generated waves representing swell are now added to the system in order to observe their effect on
314 the growing windsea.

315 **5. Effect of Monochromatic Paddle-Waves on Wind-Wave Growth**

316 To assess the effect of (following) swell on wind-wave growth we repeated the same wind forcing
317 conditions of the previous section with now long monochromatic paddle-waves generated at $X = 0$
318 m with the wave-maker. Two values of steepness of these long waves were considered: $ak = 2.7\%$
319 and $ak = 5.6\%$, with $a = H/2 = \sqrt{2m_0}$ the wave amplitude and k the wavenumber, corresponding
320 to wave frequency $f = 0.6$ Hz. In Figure 6, those wave conditions are added on the diagram
321 proposed by Le Méhauté (1976). This permits to visualize that the long waves have moderate level
322 of nonlinearity, lying in the validity domain of Stokes second order wave theory. As will be seen

323 hereafter, harmonic modes of the fundamental forcing frequency will be present in the analyzed
324 spectra.

325 In the wave tank, the addition of these regular long waves had the direct and visible effect of
326 attenuating the wind-waves. Figure 7 illustrates this interaction through the spatial evolution of
327 the variance density spectrum for the wind speed $U_{ref} = 10 \text{ m.s}^{-1}$. For that purpose, the pure
328 wind-wave spectrum is compared to the spectrum combining wind-waves and paddle-waves. The
329 semi-log scale in Figure 7 emphasizes the generation of wind-waves at high frequencies. At short
330 fetch (from 0 to 10 m), wind-wave peak frequency in the presence of long waves deviates from the
331 pure wind-wave peak frequency: the wind-wave peak frequency becomes lower as the steepness of
332 the long-wave increases. This downshift is even more pronounced at a lower wind speed (not shown
333 here). The frequency deviation from the pure windsea growth is also depicted in Figure 8 using
334 the spectral decomposition presented in Section 2.b. A possible explanation for this downshift is
335 the presence of high frequency harmonics initiating wind-wave growth at frequencies lower than
336 in the absence of paddle-waves. The induced frequency shift reduces at larger fetch and eventually
337 vanishes. Thus, the progression of the wind-wave peak towards low frequencies is slowed down in
338 the presence of long monochromatic waves.

339 Donelan (1987) drew attention to the slowed rate of progression of the paddle-modified windsea
340 peak towards low frequencies with increasing fetch. In his 100-m-long tank, the introduction of
341 long waves upshifted the windsea peak frequency at large fetch ($X \sim 70 \text{ m}$). This tendency of the
342 pure windsea peak to overtake the paddle-modified one in its progression towards low frequencies
343 could be imagined as a scenario in our case with an extended fetch: in Figure 8, an hypothetical
344 spatial extension of the $ak = 5.6 \%$ peak frequency evolution towards higher fetch would probably
345 lead to the observation of Donelan. According to him, the frequency shift previously described
346 could be due to an alteration of the dispersion relation when a paddle-wave passes through a group

347 of wind-waves, resulting in a detuning of the resonance leading to a modified nonlinear quartet
348 interaction. This hypothesis is also relevant to explain the broadening of the paddle-modified
349 wind-wave peak in its forward face (low-frequency).

350 Regarding the relative energy of wind-wave, paddle-waves broaden and flatten the corresponding
351 spectral peak (Figure 7) resulting in a total energy (m_0 , see Figure 8) smaller than the total energy
352 of pure windsea. This observation is in line with previous studies (Mitsuyasu 1966; Phillips and
353 Banner 1974; Donelan 1987). At fixed wind speed and for a given fetch, wind-wave total energy
354 decreases as the steepness of the paddle-wave increases. This dependence on steepness has been
355 related to a sheltering effect by Chen and Belcher (2000).

356 In the high frequency tail of the spectra in Figure 7, a small wind-wave harmonic can be observed
357 at about 2 times the wind-wave peak frequency, for the pure wind-wave case, and to a lesser extent
358 with paddle-waves of steepness $ak = 2.7 \%$. It is hardly noticeable with paddles-waves of steepness
359 $ak = 5.6 \%$. The decrease of this second harmonic peak as the long-wave steepness increases is a
360 consequence of the reduction of the amplitude of the main wind-wave spectral peak with increasing
361 long-wave steepness, resulting in a lower nonlinearity level of the wind wave component. Except
362 for this difference, the high frequency tail is not altered in the presence of paddle-waves. This
363 last observation is in disagreement with Donelan (1987) who noticed a higher tail for the cases
364 including paddle-waves.

365 A semi log-scale is necessary to observe the high frequency behaviour of wave-spectra but
366 differences around the spectral peaks are usually less visible. Removing the semi log-scale permits
367 to discern the location of the significant energy in the spectra. Figure 9 shows the energy transfers
368 differentiating so called “pure” paddle-waves (a) and “pure” wind-waves (b) cases from the paddle-
369 wave-plus-wind-wave combination (c) using a direct subtraction between the measured spectra.
370 The pink area is a good illustration of the interaction between long monochromatic waves and

371 short wind-waves. The wind-wave reduction previously observed appears in the negative pink area
372 between 1.25 and 2 Hz. The pink area under the first harmonic shows the amplification of the
373 monochromatic paddle-waves. A striking effect illustrated in Figure 9 is the amplification of the
374 second harmonic of the paddle-waves by the wind: negligible in Figure 9.a, the second harmonic
375 is prominent and even more amplified than the first harmonic in Figure 9.c. This amplification is
376 a consequence of the frequency of the second harmonic of the fundamental mode of the paddle-
377 waves lying in the frequency band of the wind wave peak. Though less marked, this effect also
378 manifests on the third harmonic at 1.8 Hz. In the same vein, it is observed in Figure 7 that higher-
379 order harmonics of the paddle-waves are significantly amplified (see for instance the spectra with
380 paddle-waves of steepness $ak = 5.6\%$ for fetches from 10 to 20 m, for which the third harmonic is
381 highly enhanced so has to become higher than the second harmonic. Thus, higher-order harmonics
382 plays an important role in the interaction between both wave systems. These ideal waves enable
383 a separation of the physical phenomena taking part into wave systems interactions. But adverse
384 effects such as the amplification of wave harmonics can alter the direct comparison with ocean
385 waves.

386 **6. Effect of Irregular Paddle-Waves on Wind-Wave Growth**

387 In order to consider a more realistic long-wave system representing swell, a JONSWAP-type
388 sea-state was generated in the wave tank. The spatial evolution of the bimodal sea-states with fetch
389 is compared to the pure windsea case using a spectral representation in Figure 10. In this section,
390 the steepness ak of the irregular waves is defined as $a = H_s / (2\sqrt{2}) = \sqrt{2m_0}$ and $k = k_p$. Using this
391 definition, monochromatic and irregular waves with the same steepness have the same energy.

392 As in Figure 7, the spatial evolution of spectra with fetch is shown in Figure 10. A striking effect
393 is the downshift of the wind-wave peak frequency in the presence of long irregular waves. The

394 downshift appears at the earliest stage of wind-wave growth (fetch $X = 1.99$ m in Figure 10) and
395 has the tendency to increase with increasing paddle-wave steepness. It then slightly reduces with
396 fetch but remains significant even at the maximal fetch (i.e. $X = 29.98$ m).

397 Figure 11 depicts different slopes in the non-dimensional peak-frequency evolution depending on
398 the presence of paddle-waves and their relative steepness: the progression towards low-frequency
399 is slowed down with increasing paddle-waves steepness. A likely cause for the downshift is the
400 presence of paddle-wave energy at relatively high frequencies initiating wind-wave growth at lower
401 frequencies than for the pure windsea case.

402 Regarding the wind-wave energy, a small amplification effect due to long irregular waves is
403 shown in Figure 11 for the wind speed $U_{\text{ref}} = 14 \text{ m.s}^{-1}$. This amplification, more significant at
404 short fetch, has a tendency to reduce with increasing fetch. This reflects a slower energy variation
405 with fetch in the presence of irregular paddle-waves. At lower wind speed, this small amplification
406 becomes a small reduction at the maximal fetch (see table 1).

407 Overall, the effect of irregular waves on wind-wave energy appears weaker compared to
408 monochromatic waves of the same energy. In the present study, the absence of a clear reduc-
409 tion of the windsea energy due to the presence of irregular paddle-waves is in disagreement with
410 Benetazzo et al. (2019) and Bailey et al. (2020). A plausible explanation for these diverging obser-
411 vations, based on Benetazzo et al. (2019), is an insufficient separation between the wave systems
412 leading to a misinterpretation of the spectra combining wind-waves and paddle-waves. Using
413 Figure 10 to illustrate this latter remark, if one only considers the energy at the peak frequency
414 of the pure windsea, the presence of paddle-waves indeed causes a wind-wave reduction at this
415 particular frequency. Thus, it is only by considering the downshift that one can observe wind-wave
416 energy has not been reduced but downshifted towards lower frequencies. Figure 10 in the paper of
417 Benetazzo et al. (2019) shows that the wind-wave peak frequency downshift cannot be observed in

418 their case due to the presence of the paddle-wave peak at 1 Hz. A lower paddle-wave frequency, in
419 our case, permits the observation of this downshift.

420 **7. Discussion**

421 *a. Wind-Wave Generation on Long Mechanically-Generated Waves*

422 The effect of both monochromatic and irregular long waves on windsea have been studied
423 experimentally in a wind-wave flume. Although these long-wave systems are very different in term
424 of spectral shape, their comparison in the presence of wind provides new insight about the physical
425 processes at stake in the interaction between long waves and short wind-waves.

426 In the wind-wave generation process, a first impact of paddle-waves lies in the interaction with
427 the airflow. It has been shown in Figure 3 that the vertical profile of wind speed is modified
428 in the presence of paddle-waves. This observation is not surprising since the wind stress is
429 mainly supported by waves traveling slower than the wind which is the case for both wind-waves
430 and paddle-waves in our experiments. Additionally, the use of the logarithmic profile method
431 to determine the friction velocity and the aerodynamic roughness seems questionable since the
432 presence of long waves propagating slower than the wind is prone to invalidate the analogy with the
433 airflow above a stationary rough plate. A method free from the logarithmic profile hypothesis, such
434 as the eddy-correlation method using a thin cross-X hot wire anemometer, would be more adapted
435 for the characterization of the airflow in the presence of paddle-waves; this is left for further work.
436 The other facet of this interaction lies in the amplification of paddle-waves that absorb momentum
437 from the wind.

438 The physical process, named 'sheltering effect' by Chen and Belcher (2000), mostly affects the
439 wind-wave energy and occurs especially with monochromatic paddle-waves. The main character-

440 istic differentiating these latter waves from the irregular waves is the distribution of wave energy
441 over a range of frequencies. The wave trough between two consecutive crests of the dominant wave
442 mode is much deeper with monochromatic paddle-waves than with irregular ones. In the case of
443 irregular paddle-waves, the troughs are often “filled” with other wave modes causing lower height
444 differences between crests and troughs than in the monochromatic case.

445 Regarding the wind-wave evolution in the frequency domain, irregular and monochromatic long
446 waves have the similar property to downshift the early generation frequency of the wind-waves as
447 it is visible at short fetch in Figures 7 and 10. This effect is even more pronounced with irregular
448 waves. The paddle-waves bring some initial energy at high frequencies with the high frequency
449 harmonics for the monochromatic case and the high frequency tail in the irregular case. This initial
450 energy seems to facilitate wind-wave growth at a lower frequencies than in absence of paddle-waves
451 where no initial energy is present. With irregular paddle-waves, the energy continuum brought by
452 the high frequency tail of the spectrum amplifies this property, thus initiating wind-wave growth
453 with a higher energy and a lower frequency than without paddle-waves. Thus, the wind energy
454 input at the early stage of wind-wave growth is somehow shifted towards lower frequencies and
455 added to existing waves when an initial sea state is present.

456 As it has been seen in Figure 8 and 11, the evolution of wind-wave energy and peak-frequencies
457 with fetch using log-scaled axis can be approximated by straight lines. Thus, in the same manner
458 of the previously used empirical power laws, the wind-wave growth observed in our tank can
459 be described using power laws. Table 1 gathers the power laws parameters providing a concise
460 summary of our results on wind-wave growth with and without paddle-waves. In Table 1, the
461 absolute values of coefficients c and e globally decrease with paddle-waves steepness, showing
462 that both the variations of wind-wave energy and peak-frequencies with fetch become milder.
463 Additionally, these variations are even more softened in the presence of irregular paddle-waves.

464 Several physical processes can account for the slowing down of the wind-wave energy increase
465 with fetch. At this point, the reduced wind-wave energy evolution with monochromatic paddle-
466 waves must be distinguished from the slightly amplified wind-wave energy with irregular paddle-
467 waves in comparison with the pure windsea (see Figures 8 and 11). The slowed increase of
468 wind-wave energy with monochromatic paddle-waves, that has been extensively studied in the
469 past, has been related to wind-wave enhanced dissipation (Phillips and Banner 1974), long-wave
470 sheltering effect (Chen and Belcher 2000) and nonlinear wave-wave interactions (Masson 1993).
471 However, this latter process is only significant when the ratio of long waves over short-waves
472 frequencies is less than 0.6 according to Masson (1993). This condition is not satisfied in our case
473 with the first harmonic of the monochromatic waves, yet wind-waves could be interacting with the
474 second harmonic closer to the wind wave peak (Figure 9). If an analogous analysis is performed
475 on the slowed increase of wind-wave energy with fetch in the presence of irregular waves, since
476 the sheltering effect is certainly reduced due to the spectral property, only enhanced dissipation
477 and nonlinear wave-wave interaction are possible candidates. In this latter case, Masson's ratio is
478 0.6 at maximal fetch implying a weak nonlinear interaction between wave systems. The remaining
479 candidate would be the enhanced wave breaking due to wind-wave interaction with the addition of
480 long waves orbital velocities and wind drift as formulated by Phillips and Banner (1974).

481 The slowed rate of progression of the windsea peak towards lower frequencies with increasing
482 fetch can be related to nonlinear interactions. With monochromatic paddle-waves, Donelan (1987)
483 suggested that the wind-wave energy transfer towards low frequencies might be reduced due to
484 wind-waves reduced steepness, thus nonlinearity, compared to pure windsea. This latter suggestion
485 can be illustrated in Figure 12 where the wind-wave energy is expressed as a function of the wind-
486 wave peak frequency. In this figure, wind-wave growth in the presence of paddle-waves (blue and
487 red dots respectively for monochromatic and irregular paddle-waves) are situated below the pure

488 wind-wave growth (black dots). Thus, at a fixed wind-wave energy, the corresponding wind-wave
489 peak frequencies in the presence of paddle-waves are lower than in the pure wind sea case. Since a
490 lower wave frequency relates to a lower wavenumber k (using the dispersion relation) and the wave
491 energy is proportional to the squared wave amplitude a , it appears that the wind-wave steepness
492 is reduced in the presence of paddle-waves. Additionally, Figure 12 shows that the wind-wave
493 steepness is even more lowered when irregular paddle-waves are present. This latter observation
494 suggests that nonlinear interactions are a good candidate to explain the slowed decrease of wind
495 wave peak frequency with fetch in the case with irregular waves.

496 *b. Relation to Wind Waves Growth at Prototype Scale*

497 The extent at which our experimental results, can be generalized at natural scale is discussed in the
498 following. As mentioned in Introduction, the main difference between laboratory and natural scale
499 measurements lies in the wave age of the swell. While the wind velocity conditions produced during
500 the experiment are close to that observed in natural conditions, the mechanically-generated waves
501 representing swell are significantly shorter, thus slower, than the swell conditions encountered in
502 the ocean. Thus, an appropriate scaling was performed to compare our experiments with equivalent
503 natural scale observations. Being aware of the main differences in term of wave age, qualitative
504 comparisons permitted to draw tendencies about the physical processes involved in the interaction
505 between swell and wind-waves at natural scale.

506 First, an effort was devoted to the determination of the wind friction velocity in order to perform an
507 accurate scaling. Some doubts were formulated regarding the measuring device and the pertinence
508 of the logarithmic profile method to determine the friction velocity in the presence of paddle-waves.
509 Using ocean buoys measurements, Vincent et al. (2019) showed that the friction velocity tends to
510 increase with swell steepness especially at low wind speeds. A similar trend is observed in Figure

511 3 as the friction velocity increases with the long paddle-waves. To confirm the similarities between
512 both scales, it would be necessary to use a method free from the logarithmic profile analogy for
513 the wind profile characterization.

514 As it was highlighted in section 4, wind-wave growth (without paddle-waves) in laboratories
515 shows similarities with that at natural scale. To observe these similarities, laboratory wind-waves
516 must be long enough to be free from surface tension effects. Then, the wind-wave energy and
517 peak frequency (Figure 4) were close to Kahma and Calkoen's empirical relations, representing
518 wind-wave growth at natural scale, but slightly deviated in terms of variations with increasing
519 fetch.

520 The introduction of paddle-waves, representing swell, significantly modifies the wind-wave field.
521 First, monochromatic paddle-waves cause a reduction of wind-wave energy. This reduction has
522 received numerous interpretations that reached an agreement on the fact that the physical processes
523 responsible for that reduction are proper to steep short waves (equivalent to paddle-waves in natural
524 reservoirs) traveling slower than the wind (i.e. $C \ll U_{10}$). This wind-wave reduction phenomenon
525 was used to design a reduced wind input model for high frequencies waves (i.e. waves with
526 a wave age equivalent to paddle-wave) and high winds in Ardhuin et al. (2010). Some gray
527 areas remain on the role played by the monochromatic wave harmonics in the modification of the
528 wind-wave growth. The prominence of these harmonics is principally inherent in laboratory steep
529 monochromatic paddle-waves and might damage the relation with wind-waves at natural scale.

530 Secondly, the wind-wave peak frequency and its variations with increasing fetch are modified
531 in the presence of either irregular or, to a lower extent, monochromatic paddle-waves. In Figures
532 8 and 11, the wind-wave peak frequency variations with fetch are closer to Kahma and Calkoen's
533 than to Mitsuyasu and Rikiishi's power laws although the latter is specific for laboratory wind-wave
534 growth. In Table 1, the same tendency can be observed by comparing the power law coefficient

535 e in the presence of paddle waves with the corresponding coefficient in Kahma and Calkoen's
536 law ($e = -0.26$). Furthermore, in the presence of irregular paddle-waves, wind-wave energy
537 evolution with increasing fetch follows this agreement with Kahma and Calkoen relations. This
538 accordance can be observed in Figure 11 or by comparing the power law coefficient c in Table
539 1 with the coefficient $c = 0.85$ of Kahma and Calkoen. Finally, irregular paddle-waves seem to
540 restore wind-wave growth as it is observed at natural scale.

541 **8. Conclusion**

542 A series of experiments were carried out at IRPHÉ/Pythéas wind-wave tank in Marseilles. The
543 interactions between long paddle-waves, representing swell, and short wind-waves were investi-
544 gated with both monochromatic and irregular paddle-waves. An analysis was performed in order
545 to identify the interaction mechanisms that can be transported at prototype scale.

546 Wind-wave growth was studied in absence of paddle-waves to assess the similarities with existing
547 experiments. It was found that, after the young wind-waves emancipate from the gravity-capillary
548 state, wind-wave growth is in agreement with laboratory based empirical laws but differ from more
549 general laws (i.e. laws valid at prototype scale) in terms of variations with fetch.

550 By calculating the vertical profile of the wind horizontal velocity using the logarithmic profile
551 method, the friction velocity had a tendency to increase in the presence of paddle-waves. However,
552 the measurements uncertainties added to the limited validity of the logarithmic profile method
553 to characterize the airflow in the presence of long paddle-waves prevented a more quantitative
554 analysis. The use of a more accurate method, such as the eddy correlation method, is let for further
555 work.

556 The interactions between wind and paddle-waves have repercussions on the wave systems. The
557 paddle-waves are amplified by the wind which echoes back to the sheltering effect highlighted by

558 Chen and Belcher (2000). With monochromatic paddle-waves, this shelter effect seems to affect
559 wind-wave growth by reducing the quantity of momentum available for wind-wave generation.
560 In this latter case, the wind mostly impacts the wind-wave energy. Thus, the wind-wave peak
561 frequency evolution with fetch is similar to wind only conditions, resulting in a reduced wind-wave
562 steepness in the presence of monochromatic paddle-waves.

563 The effect of irregular paddle-waves on wind-wave growth is quite different since the wind-
564 wave parameter affected by this interaction is mostly the wind-wave peak frequency. The energy
565 continuum brought by the paddle-waves high frequency tail initiates wind-wave growth at a lower
566 frequency than in the absence of paddle-waves. Thus, it was found that the irregular low frequency
567 waves downshift wind-wave peak frequency in a significant manner. The wind-wave energy being
568 only slightly impacted by comparison with the peak-frequency, irregular paddle-waves reduces
569 wind-wave steepness even more than in the monochromatic paddle-wave case.

570 The similarities between the action of monochromatic and irregular paddle-waves on wind-wave
571 growth lie in the wind-wave energy and peak frequencies reduced variations with fetch. It is
572 interesting to note that most laboratory measurements, for example Mitsuyasu and Rikiishi (1978),
573 display an accelerated wind-wave growth (i.e. wind-wave energy increases faster and the peak
574 frequency reduces faster) by comparison with ocean measurements, illustrated here by Kahma and
575 Calkoen (1992)'s empirical law. Especially with irregular paddle-waves, which is a more faithful
576 reproduction of a typical ocean sea-state, wind-wave growth is somehow in accordance with
577 Kahma and Calkoen (1992)'s law. A result from this latter observation is that wind-wave growth
578 in laboratories seems closer to wind-wave growth at prototype scale when irregular paddle-waves
579 are present.

580 Finally, our experiments provide a valuable database for validating a spectral wave model. From
581 this database, spectral wave model performances can be assessed under generic conditions for

582 both wind and wave forcing. Using the separation of the physical mechanisms at the root of
583 wind-wave generation in the spectral energy balance equation (1), the ability of the spectral wave
584 model in reproducing wind-wave growth with and without paddle-waves might enable to identify
585 the mechanisms at the origin of the wave systems interactions observed in laboratory. Ultimately,
586 the use of a spectral wave model may help to evaluate the extent at which the mechanisms observed
587 in laboratories can be transposed to prototype scale.

588 *Acknowledgments.* Antoine Villefer acknowledges the financial support of his PhD research pro-
589 gram provided by the French ANRT (Association Nationale de la Recherche et de la Technologie)
590 with CIFRE grant number 2019-1257. The authors thanks Maria-Joao Teles (EDF R&D LNHE)
591 and Jeffrey Harris (ENPC/LHSV) for many fruitful discussions in the course of this study.

592 *Data availability statement.*

593 **References**

- 594 Ardhuin, F., and Coauthors, 2010: Semiempirical Dissipation Source Functions for Ocean Waves.
595 Part I: Definition, Calibration, and Validation. *Journal of Physical Oceanography*, **40**, 1917–
596 1941.
- 597 Bailey, T., L. Ross, M. Bryant, and D. Bryant, 2020: Predicting Wind Wave Suppression on
598 Irregular Long Waves. *Journal of Marine Science and Engineering*, **8**, 619.
- 599 Benetazzo, A., L. Cavaleri, H. Ma, S. Jiang, F. Bergamasco, W. Jiang, S. Chen, and F. Qiao, 2019:
600 Analysis of the effect of fish oil on wind waves and implications for air–water interaction studies.
601 *Ocean Science*, **15** (3), 725–743.
- 602 Chen, G., and S. E. Belcher, 2000: Effects of Long Waves on Wind-Generated Waves. *Journal of*
603 *Physical Oceanography*, **30**, 2246–2256.

- 604 Coantic, M., A. Ramamonjiarisoa, P. Mestayer, F. Resch, and A. Favre, 1981: Wind-water tunnel
605 simulation of small-scale ocean-atmosphere interactions. *Journal of Geophysical Research*, **86**,
606 6607–6626.
- 607 Donelan, M., 1987: The effect of swell on the growth of wind waves. *Johns Hopkins APL Technical*
608 *Digest*, Vol. 8, 18–23.
- 609 Donelan, M., W. Drennan, and K. Katsaros, 1997: The Air-Sea Momentum Flux in Conditions of
610 Wind Sea and Swell. *Journal of Physical Oceanography*, **27**, 2087–2099.
- 611 Donelan, M. A., B. K. Haus, W. J. Plant, and O. Troianowski, 2010: Modulation of short wind
612 waves by long waves. *Journal of Geophysical Research: Oceans*, **115**, C10 003.
- 613 Dorn, W. G. V., 1966: Boundary dissipation of oscillatory waves. *Journal of Fluid Mechanics*,
614 **24 (4)**, 769–779.
- 615 Hasselmann, K., and Coauthors, 1973: Measurements of wind-wave growth and swell decay during
616 the Joint North Sea Wave Project (JONSWAP). *Deut. Hydrogr. Z.*, **8**, 1–95.
- 617 Hwang, P. A., H. García-Nava, and F. J. Ocampo-Torres, 2011: Observations of Wind Wave
618 Development in Mixed Seas and Unsteady Wind Forcing. *Journal of Physical Oceanography*,
619 **41**, 2343–2362.
- 620 Janssen, P. A. E. M., 2004: *The Interaction of Ocean Waves and Wind*. Cambridge University
621 Press.
- 622 Kahma, K. K., and C. J. Calkoen, 1992: Reconciling discrepancies in the observed growth of
623 wind-generated waves. *Journal of Physical Oceanography*, **22 (12)**, 1389 – 1405.
- 624 Kitaigorodskii, S., 1961: Application of the theory of similarity to the analysis of wind generated
625 wave motion as a stochastic process. *Izv. Geophys. Ser.*, **1**, 105–117.

- 626 Komen, G. J., L. Cavaleri, M. Donelan, K. Hasselmann, S. Hasselmann, and P. A. E. M. Janssen,
627 1994: *Dynamics and Modelling of Ocean Waves*. Cambridge University Press.
- 628 Le Méhauté, B., 1976: *An Introduction to Hydrodynamics and Water Waves*. Springer Study
629 Edition, Springer Berlin Heidelberg.
- 630 Mackay, E., 2011: Modelling and Description of Omnidirectional Wave Spectra. *European Wave
631 & Tidal Energy Conference EWTEC 2011*, University of Southampton, UK.
- 632 Masson, D., 1993: On the Nonlinear Coupling between Swell and Wind Waves. *Journal of Physical
633 Oceanography*, **23**, 1249–1258.
- 634 Miles, J. W., 1957: On the generation of surface waves by shear flows. *Journal of Fluid Mechanics*,
635 **3 (2)**, 185–204.
- 636 Mitsuyasu, H., 1966: Interactions between Water Waves and Wind (1). *Rep. Inst. Appl. Mech.
637 Kyushu Univ.*, **14**, 67–88.
- 638 Mitsuyasu, H., and K. Rikiishi, 1978: The growth of duration-limited wind waves. *Journal of
639 Fluid Mechanics*, **85 (4)**, 705–730.
- 640 Mitsuyasu, H., and Y. Yoshida, 1991: The Effect of Swell on the Growth of Wind Waves. *Elsevier
641 Oceanography Series*, **54**, 381–392.
- 642 Monin, A. S., and A. M. Obukhov, 1954: Basic laws of turbulent mixing in the surface layer of the
643 atmosphere. *Tr. Akad. Nauk SSSR Geophys. Inst.*, **24**, 163–187.
- 644 Phillips, O. M., and M. L. Banner, 1974: Wave breaking in the presence of wind drift and swell.
645 *Journal of Fluid Mechanics*, **66**, 625–640.
- 646 Shemer, 2019: On Evolution of Young Wind Waves in Time and Space. *Atmosphere*, **10 (9)**, 562.

- 647 Toba, Y., 1997: The 3/2-Power Law for Ocean Wind Waves and its Applications. *Advances in*
648 *Coastal and Ocean Engineering*, World Scientific, 31–65.
- 649 Vincent, C. L., J. Thomson, H. C. Graber, and C. O. Collins III, 2019: Impact of swell on the
650 wind-sea and resulting modulation of stress. *Progress in Oceanography*, **178**, 102–164.
- 651 Wright, J. W., 1976: The Wind Drift and Wave Breaking. *Journal of Physical Oceanography*, **6**,
652 402–405.

653 **LIST OF TABLES**

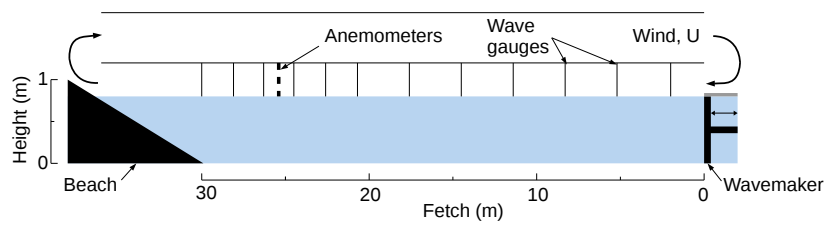
654 **Table 1.** Wind characteristics and corresponding power law coefficients representing the
655 fetch dependence of windsea peak frequency and energy ($m_0^* = b(X^*)^c$ and
656 $f_p^* = d(X^*)^e$). The lines with bold characters refer to the pure windsea cases. . . . 33

U_{ref} (m.s ⁻¹)	6	10	14	
U_{10} (m.s ⁻¹)	9	13	20	
u_{\star} (m.s ⁻¹)	0.31	0.48	0.88	
$z_0 \times 10^4$ (m)	1.4	1.6	9.3	
Swell type	ak (%)	$(b \times 10^4, c)$		
Monochromatic	5.6	(0.13, 1.28)	(0.59, 1.05)	-
	2.7	(2.00, 0.99)	(0.31, 1.29)	(4.61, 0.82)
	0.0	(0.02, 1.64)	(0.11, 1.50)	(0.52, 1.30)
Irregular	2.7	(2.16, 1.01)	(0.96, 1.17)	(1.27, 1.18)
	4.1	(2.68, 1.01)	(7.56, 0.90)	(5.47, 0.91)
Swell type	ak (%)	(d, e)		
Monochromatic	5.6	(0.60, -0.28)	(0.64, -0.30)	-
	2.7	(1.68, -0.42)	(1.27, -0.38)	(0.86, -0.33)
	0.0	(3.46, -0.50)	(1.36, -0.39)	(0.89, -0.33)
Irregular	2.7	(0.06, -0.01)	(0.28, -0.20)	(0.34, -0.22)
	4.1	(0.11, -0.11)	(0.07, -0.02)	(0.21, -0.14)

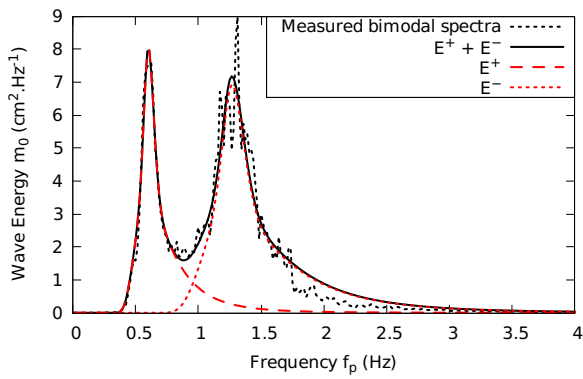
657 TABLE 1. Wind characteristics and corresponding power law coefficients representing the fetch dependence of
658 windsea peak frequency and energy ($m_0^* = b(X^*)^c$ and $f_p^* = d(X^*)^e$). The lines with bold characters refer to the
659 pure windsea cases.

LIST OF FIGURES

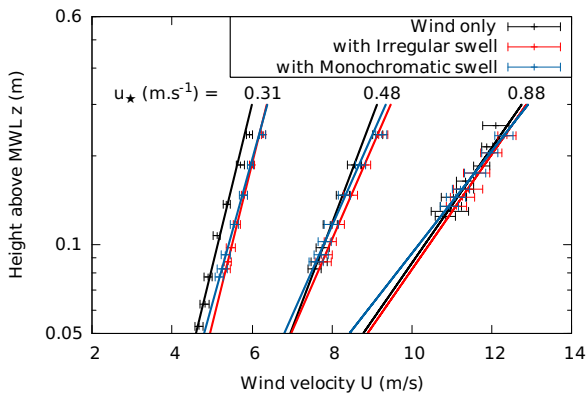
660		
661	Fig. 1.	Sketch of the IRPHÉ/Pythéas wind-wave tank facility showing the location of the measuring devices. The vertical exaggeration is $\times 5$ 35
662		
663	Fig. 2.	Example of spectral separation for a spectrum obtained at a 30-m-fetch with a wind of 10 m.s^{-1} in presence of irregular long waves of 2.7 % steepness. E^+ and E^- are respectively the JONSWAP fit of the higher and the lower peaks. 36
664		
665		
666	Fig. 3.	Vertical profiles of the averaged horizontal wind velocity with and without paddle-waves associated logarithmic fits. The corresponding friction velocities values (mean slope of the fitted lines) are indicated for each wind only cases. 37
667		
668		
669	Fig. 4.	Variations of dimensionless wave energy and peak frequency with dimensionless fetch for different reference wind speeds (U_{ref}) compared to empirical laws. 38
670		
671	Fig. 5.	Variations of the wind-wave dimensionless energy with the dimensionless peak frequency for different equivalent wind speed (U_{ref}) compared to variations according to Toba's 3/2 law (10). 39
672		
673		
674	Fig. 6.	Representation of regular paddle-wave conditions on Le Méhauté's diagram (Le Méhauté 1976). 40
675		
676	Fig. 7.	The spatial evolution of the variance density spectrum with and without regular paddle-waves of steepness ak and peak frequency 0.6 Hz for a wind speed $U_{\text{ref}} = 10 \text{ m.s}^{-1}$ 41
677		
678	Fig. 8.	The spatial evolution of wind-wave energy and peak frequency with and without regular paddle-waves of steepness ak and peak frequency 0.6 Hz for a wind speed $U_{\text{ref}} = 10 \text{ m.s}^{-1}$ 42
679		
680	Fig. 9.	Pure paddle-wave spectrum E_p (a) and pure wind-wave spectra E_w (b) by comparison with the bimodal spectrum E_{w+p} (c) with monochromatic paddle-waves of steepness $ak = 2.7 \%$ and peak frequency 0.6 Hz at fetch of 30 m for a wind speed $U_{\text{ref}} = 10 \text{ m.s}^{-1}$. The pink area is the difference between the bimodal spectrum E_{w+p} and the sum of the pure spectra $E_w + E_p$ 43
681		
682		
683		
684	Fig. 10.	The spatial evolution of the variance density frequency spectrum with and without irregular paddle-waves of steepness ak and peak frequency 0.6 Hz for a wind speed $U_{\text{ref}} = 14 \text{ m.s}^{-1}$ 44
685		
686	Fig. 11.	The spatial evolution of wind-wave energy and peak frequency with and without irregular paddle-waves of steepness ak and peak frequency 0.6 Hz for a wind speed $U_{\text{ref}} = 14 \text{ m.s}^{-1}$ 45
687		
688	Fig. 12.	Variations of the wind-waves dimensionless energy with the dimensionless peak frequency for different reference wind speeds (squares: $U_{\text{ref}} = 6 \text{ m.s}^{-1}$, circles: $U_{\text{ref}} = 10 \text{ m.s}^{-1}$, triangles: $U_{\text{ref}} = 14 \text{ m.s}^{-1}$) compared to variations according to Toba's 3/2 law. 46
689		
690		



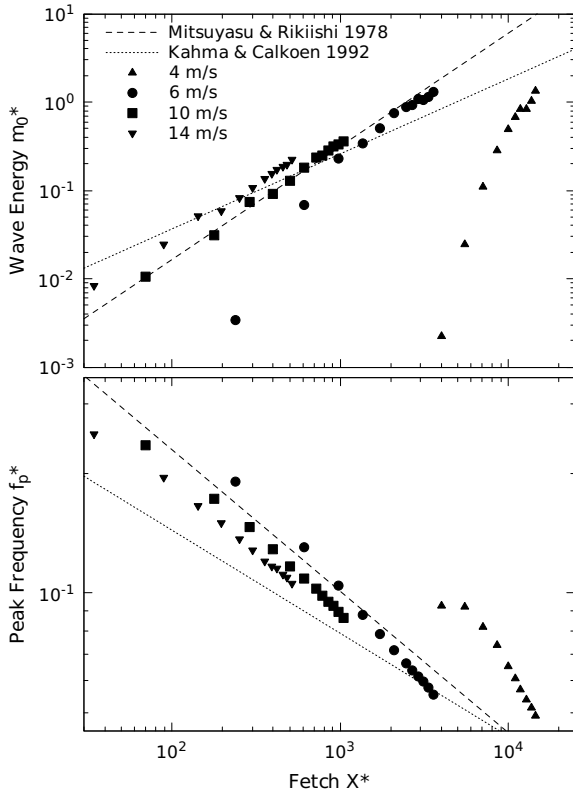
691 FIG. 1. Sketch of the IRPHÉ/Pythéas wind-wave tank facility showing the location of the measuring devices.
 692 The vertical exaggeration is $\times 5$.



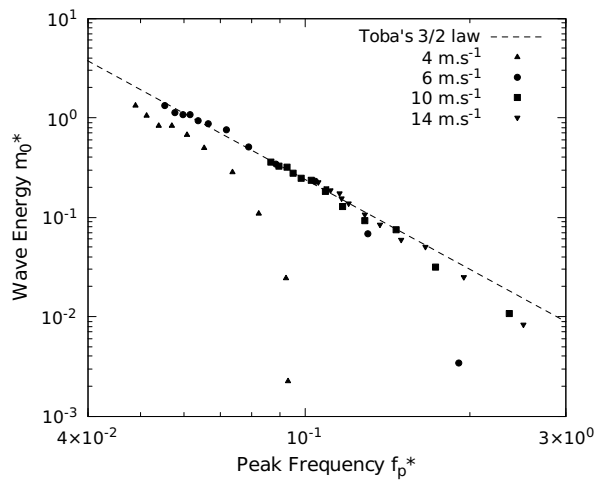
693 FIG. 2. Example of spectral separation for a spectrum obtained at a 30-m-fetch with a wind of $10 \text{ m}\cdot\text{s}^{-1}$ in
 694 presence of irregular long waves of 2.7 ‰ steepness. E^+ and E^- are respectively the JONSWAP fit of the higher
 695 and the lower peaks.



696 FIG. 3. Vertical profiles of the averaged horizontal wind velocity with and without paddle-waves associated
 697 logarithmic fits. The corresponding friction velocities values (mean slope of the fitted lines) are indicated for
 698 each wind only cases.



699 FIG. 4. Variations of dimensionless wave energy and peak frequency with dimensionless fetch for different
 700 reference wind speeds (U_{ref}) compared to empirical laws.



701 FIG. 5. Variations of the wind-wave dimensionless energy with the dimensionless peak frequency for different
 702 equivalent wind speed (U_{ref}) compared to variations according to Toba's 3/2 law (10).

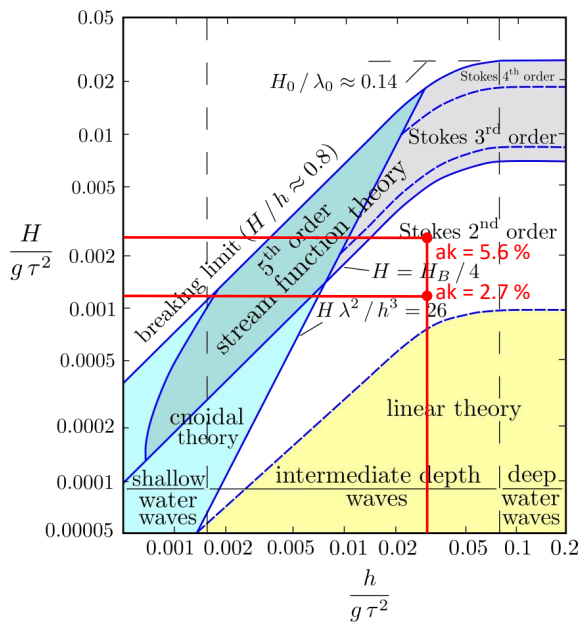
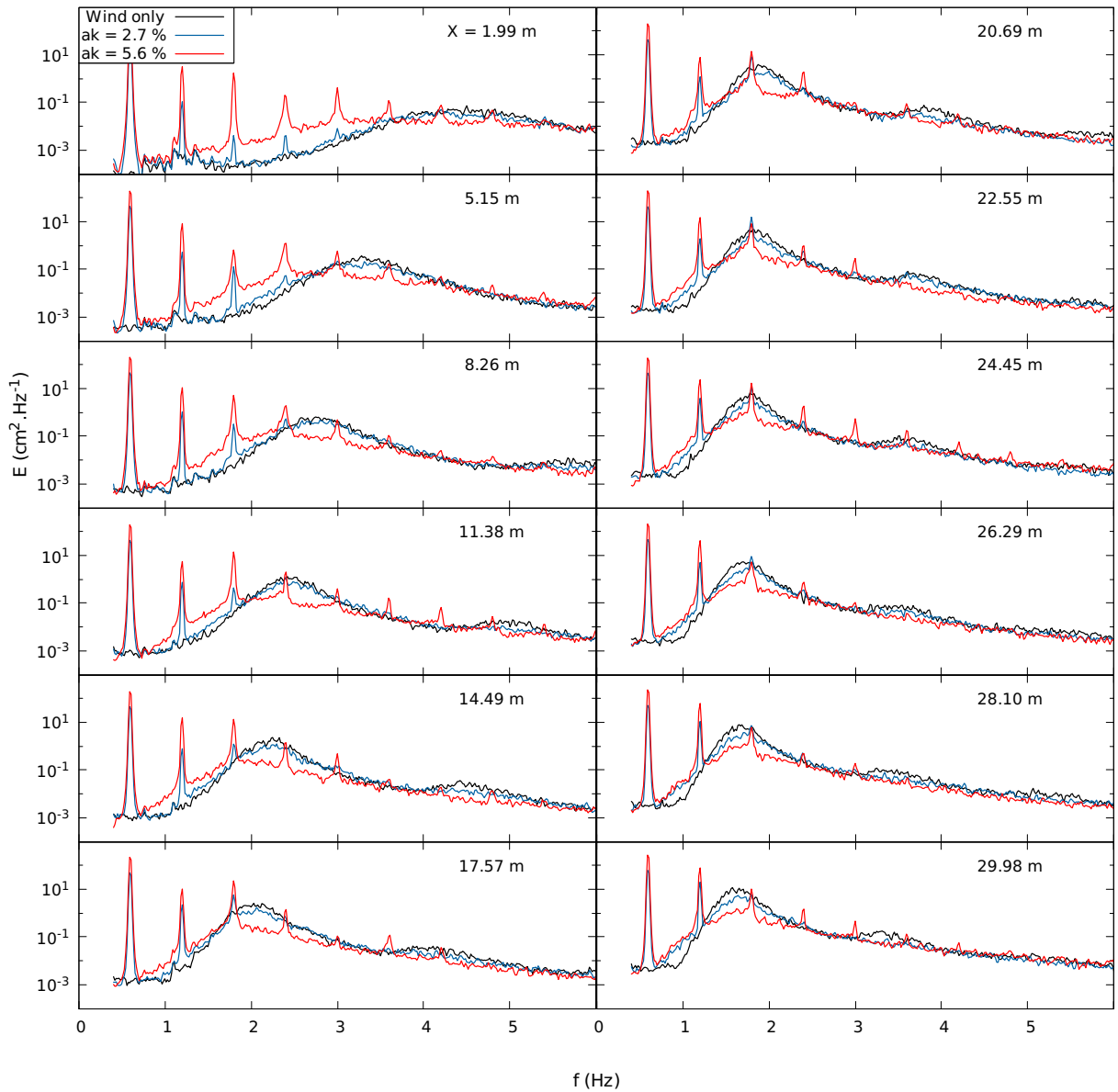
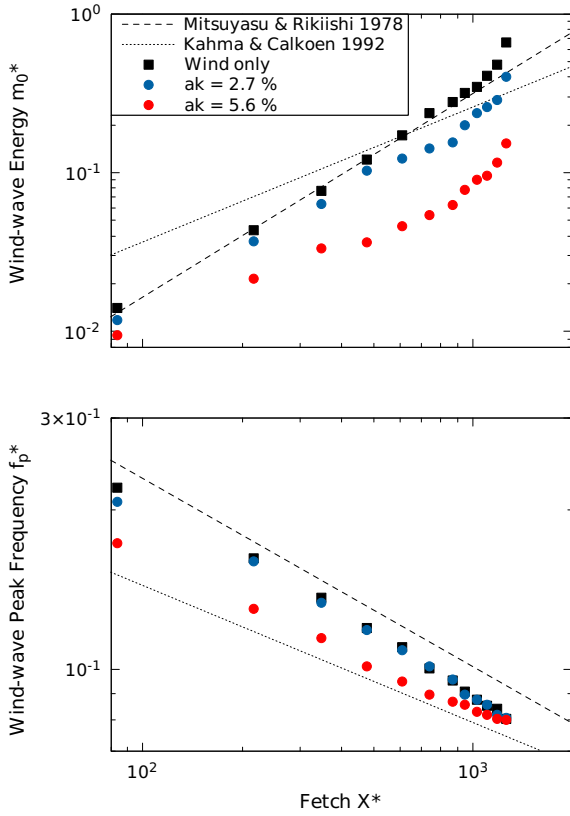


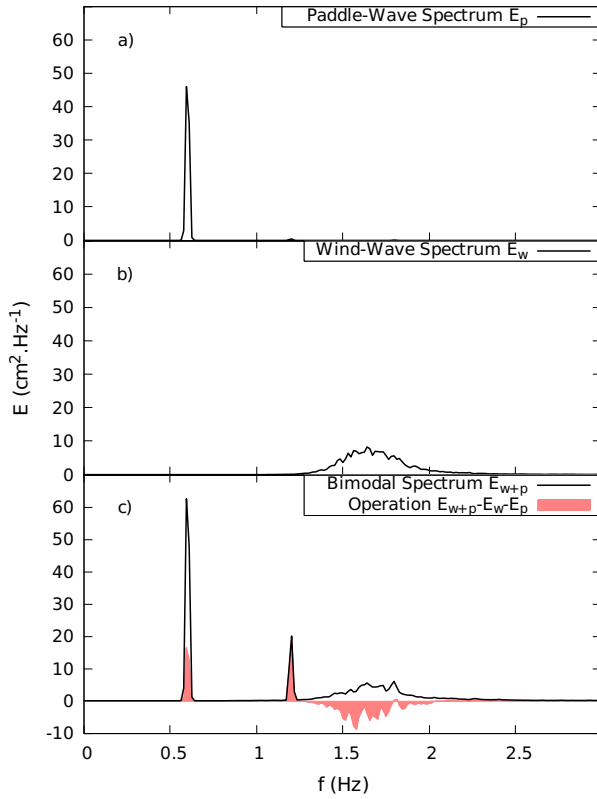
FIG. 6. Representation of regular paddle-wave conditions on Le Méhauté's diagram (Le Méhauté 1976).



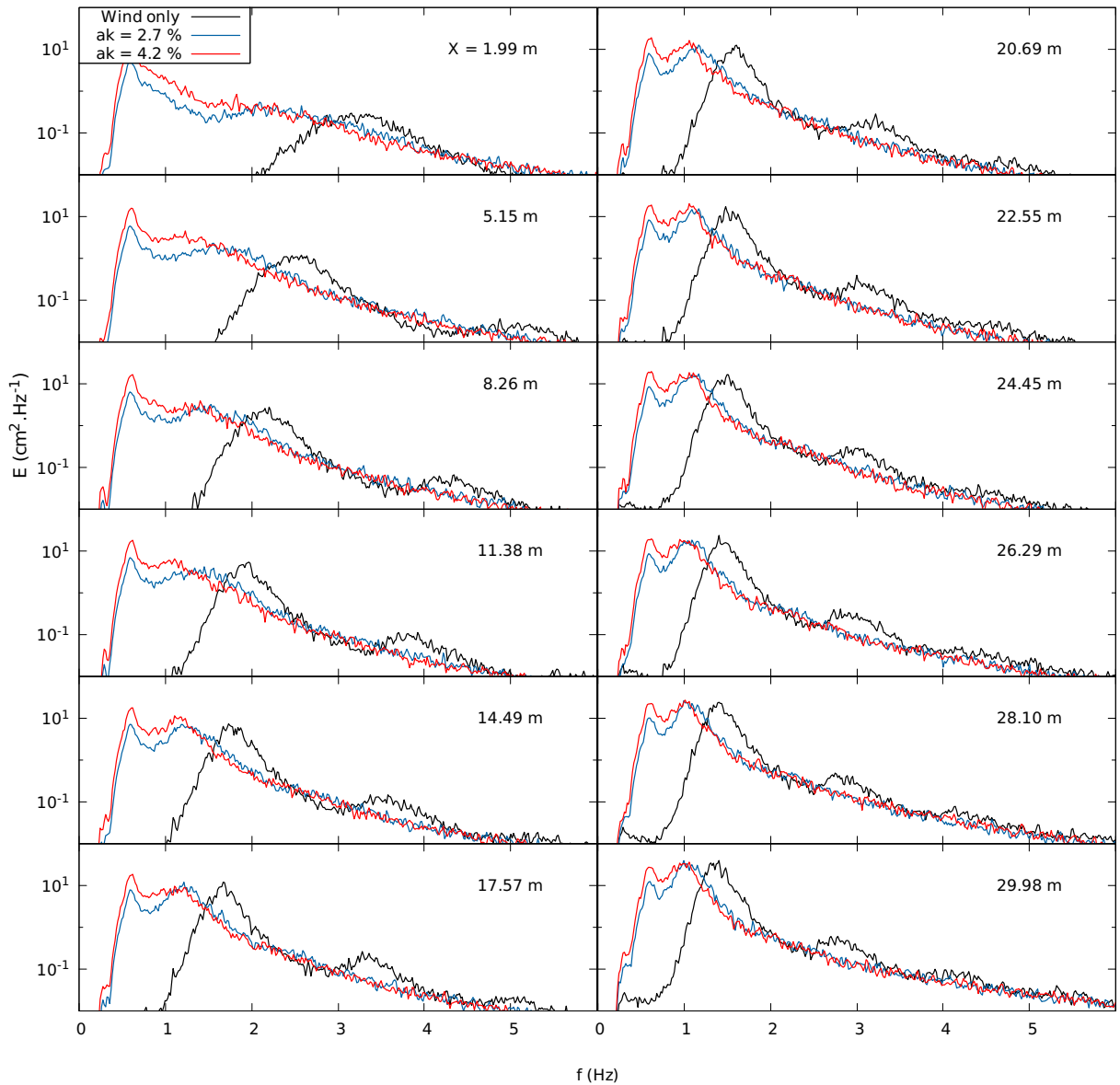
703 FIG. 7. The spatial evolution of the variance density spectrum with and without regular paddle-waves of
 704 steepness ak and peak frequency 0.6 Hz for a wind speed $U_{\text{ref}} = 10 \text{ m}\cdot\text{s}^{-1}$.



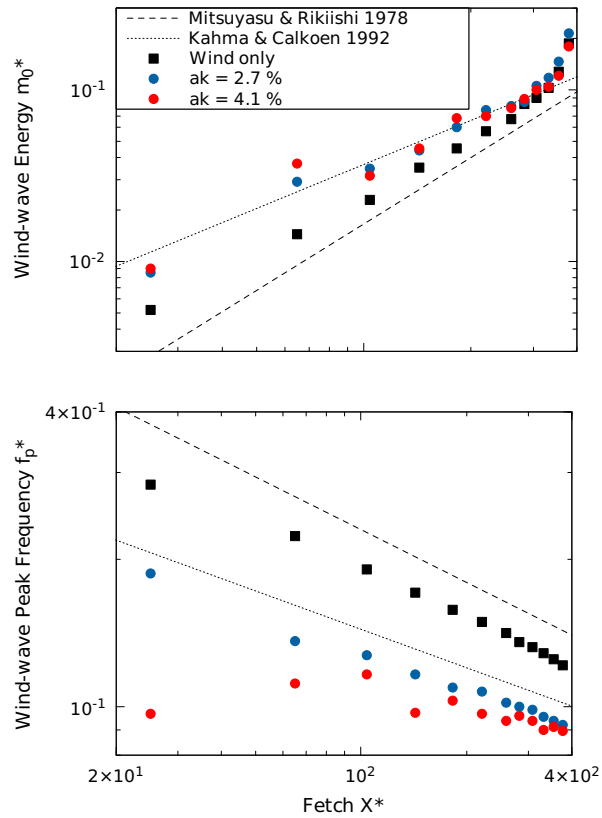
705 FIG. 8. The spatial evolution of wind-wave energy and peak frequency with and without regular paddle-waves
 706 of steepness ak and peak frequency 0.6 Hz for a wind speed $U_{\text{ref}} = 10 \text{ m.s}^{-1}$.



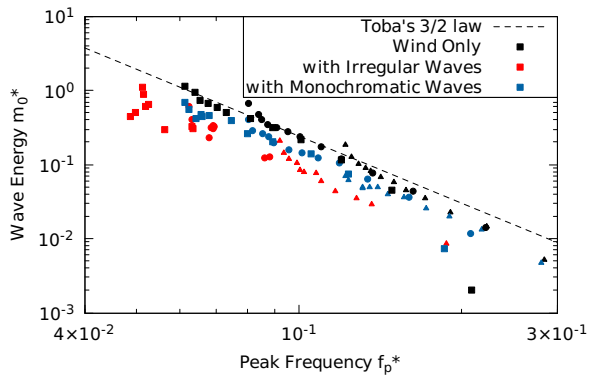
707 FIG. 9. Pure paddle-wave spectrum E_p (a) and pure wind-wave spectra E_w (b) by comparison with the bimodal
 708 spectrum E_{w+p} (c) with monochromatic paddle-waves of steepness $ak = 2.7\%$ and peak frequency 0.6 Hz at
 709 fetch of 30 m for a wind speed $U_{\text{ref}} = 10 \text{ m}\cdot\text{s}^{-1}$. The pink area is the difference between the bimodal spectrum
 710 E_{w+p} and the sum of the pure spectra $E_w + E_p$.



711 FIG. 10. The spatial evolution of the variance density frequency spectrum with and without irregular paddle-
 712 waves of steepness ak and peak frequency 0.6 Hz for a wind speed $U_{\text{ref}} = 14 \text{ m}\cdot\text{s}^{-1}$.



713 FIG. 11. The spatial evolution of wind-wave energy and peak frequency with and without irregular paddle-
 714 waves of steepness ak and peak frequency 0.6 Hz for a wind speed $U_{\text{ref}} = 14 \text{ m}\cdot\text{s}^{-1}$.



715 FIG. 12. Variations of the wind-waves dimensionless energy with the dimensionless peak frequency for
 716 different reference wind speeds (squares: $U_{ref} = 6 \text{ m.s}^{-1}$, circles: $U_{ref} = 10 \text{ m.s}^{-1}$, triangles: $U_{ref} = 14 \text{ m.s}^{-1}$)
 717 compared to variations according to Toba's 3/2 law.